Technische Universität München
Lehrstuhl für Fluidmechanik
o. Prof. Dr.-Ing. habil. Dr. h.c. Rudolf Schilling

**JASS 2009-Joint Advanced Student School, St. Petersburg, 29.03-7.4.2009**
**Numerical Simulation in Turbomachinery**

# Numerical simulation of pressure oscillations in Francis turbine runners

Magnoli M.V.
Technische Universität München,
Lehrstuhl für Fluidmechanik,
D-85747 Garching Germany

**Contents**

## Abstract

A numerical study of the real flow through a Francis turbine having a specific speed $n_{q_{opt}} = 80,3 \text{ min}^{-1}$ was carried out to predict the pressure pulsations induced by the interaction between rotor and stator, as well as by the draft tube vortex rope and by the von Kármán vortices at the runner blades trailing edges.

The reason for this study is to accurately predict the dynamic flow behaviour, allowing more precise investigations of especially the runner fatigue strength and durability, based on the spectrum of the evaluated pressure pulsations at several operating points.

The numerical computations were first performed using the in-house CFD-Code NS3D and studying the influence of the mesh density, interpolation schemes, turbulence models and prescribed turbulence intensity, at the computational domain inlet, as well as the formulation of the boundary conditions at the domain outlet. Afterwards, flow computations considering the flow through the blading, i.e. stay vanes, wicket gates and runner, as well as through the draft tube were carried out also by means of the commercial code CFX, using adequate interface models for coupling the flow through rotor and stator of the Francis Turbine.

The results obtained from NS3D and CFX computations showed excellent agreement and coincided with the available experimental data.

Besides the computations carried out on the basis of the Unsteady Reynolds-Averaged Navier-Stokes (URANS) formulation of the fluid flow equations, hybrid simulations, partly based on Large Eddy Simulation (LES) techniques, such as the Detached Eddy Simulation (DES) and Scale Adaptive Simulation (SAS) were performed, computing only the very large eddies and modelling the smaller ones.

Finally, the results of the current flow simulation will be used in the future for a Computational Structural Analysis (CSA) on the basis of the pressure dynamic loading, in order to study the influence of the rotor-stator interaction, draft tube instabilities and vortex shedding on the fatigue strength and durability of the considered Francis runner.

# Contents

# Nomenclature

## Roman Letters

| | |
|---|---|
| $C_p$ | Pressure coefficient |
| $H$ | Net head |
| $Q'_1$ | Dimensionless volume flow |
| $P$ | Fourier transform of pressure |
| $T$ | Machine revolution period |
| $T'_1$ | Dimensionless runner torque |
| | |
| $f$ | Frequency |
| $f_n$ | Machine revolution frequency |
| $g$ | Gravity acceleration |
| $n'_1$ | Dimensionless rotation speed |
| $p$ | Pressure |
| $s$ | Dimensionless coordinate running along the blade from the leading edge to the trailing edge |
| $t$ | Time |
| $u$ | Dimensionless coordinate running along the blade from the pressure side trailing edge to the suction side trailing edge |
| $v$ | Dimensionless coordinate running along the blade from crown to band |
| $y^+$ | Dimensionless sublayer-scaled distance |

## Greek Letters

| | |
|---|---|
| $\Delta$ | Oscillation amplitude, i.e. half peak to peak value |
| | |
| $\eta$ | Turbine efficiency |
| $\rho$ | Density |

## Overhead Symbols

| | |
|---|---|
| $\bar{}$ | Time-average |

## Subscripts

| | |
|---|---|
| $_{opt}$ | optimum operation point |

### Abbreviations

| | |
|---|---|
| BCGSTAB | Biconjugate gradient stabilized method |
| CDS | Central difference scheme |
| CFD | Computational fluid dynamics |
| CFX | ANSYS Inc., ANSYS-CFX Release 11.0 |
| CSA | Computational structural analysis |
| DES | Dettached eddy simulation |
| LCL | Turbulence model according to Lien, Chen and Leschziner [11] |
| LES | Large eddy simulation |
| MINMOD | Interpolation scheme according to Harten [8] |
| NS3D | Three-dimensional Navier-Stokes flow computation |
| QUICK | Quadratic upwind interpolation |
| SAS | Scale adaptive simulation |
| SST | Shear stress transport |
| UDS | Upwind difference scheme |
| URANS | Unsteady Reynolds-averaged Navier-Stokes equations |

# 1 Introduction

Pressure pulsations, flow instabilities and vortex shedding are common, mostly undesirable, transient phenomena in Francis turbines with high specific speed. The consequent pressure oscillations are at the origin of the dynamic loads, which actuate over the turbine runner and which may lead, in some cases, to its mechanical failure [4, 7]. The ability to predict the pressure oscillation field in the fluid offers the possibility to accurately simulate the runner structural stresses, fatigue strength and durability, with the aim to avoid the occurrence of mechanical failures during the machine operation.

The experimental measurement of the oscillating pressure field, during the model test, is not common, due to the necessary elaborated experimental setup and equipments [3] and the associated test duration and costs. At present, it constitutes no regular practice for ordinary model tests and it has mainly been performed in specific research projects, e.g. [10, 14]. Up to now, the oscillating pressure field, for the computation of the dynamic structural stresses, has normally been simply approximated by a percentage of the stationary pressure field or based on scarce prototype measurements [7, 9]. Therefore, the possibility of systematically simulating the pressure dynamic field with CFD models and using it as input for a structural finite element analysis can represent a progress in the strength calculation of the runner.

The first step in the flow numerical simulation was the generation of the CFD model of the complete turbine, as long as, some of the transient effects, such as the rotor-stator interaction and the flow instabilities in the draft tube diffusor, are originated from the interaction between different machine components. After it, the numerical parameters of the CFD model were optimized through the comparison with model test experimental results. As far as transient effects are involved in the flow simulation, the adopted turbulence model becomes an issue and it might affect the results quality. Hence, the URANS, SAS [13] and DES [16] turbulence models were tested. Finally, the simulated transient results, obtained for selected operating points, are presented and discussed.

Special attention was dedicated to the vortex shedding phenomenon at the runner blades trailing edge. Although it has already been identified as one of the concurrent causes of runner cracks [7], its study in hydraulic turbines runners is still limited, being restricted to extrapolations of simplified geometry simulations [1, 2, 15].

## 2 Numerical Model

The numerical model shall reproduce as accurately as possible the model behaviour at the test rig. Therefore, numerous numerical schemes and parameters were tested and verified with the available experimental results. The model accuracy was assessed on terms of its agreement with the measured head, flow, torque and efficiency. To test the numerical model accuracy, 5 different operating points in the machine hill chart were chosen, corresponding to optimum, rated, normal operation, partial load at high head and at low head. This validation step is considered to be absolutely necessary, in order to achieve reliable numerical results for the intended pressure pulsations simulation. The tests and the final simulations were carried out both on the NS3D code, developed by the Institute of Fluid Mechanics (FLM) from the Munich University of Technology (TUM), and on the commercial code CFX from ANSYS.

The first step in the numerical model preparation was the mesh generation. As long as an important part of the pressure oscillations arises from the interaction between the stationary and rotating components, the complete machine was simulated and the computational grid considered all the machine components: spiral case, stay vanes, guide vanes, runner and draft tube. The single components were separately meshed, using their own appropriate mesh strategy and using exclusively structured hexahedral grids. They were coupled together for the numerical simulation with non-matching interfaces. The grid for the complete machine simulation contains slightly more than 6 million cells. The stay vanes, guide vanes and runner were meshed using the IDS software, also developed by the FLM, while the spiral case and the draft tube made use of the commercial code ICEM from ANSYS. The mesh and typical simulation results are exemplified in Figure 2.1.

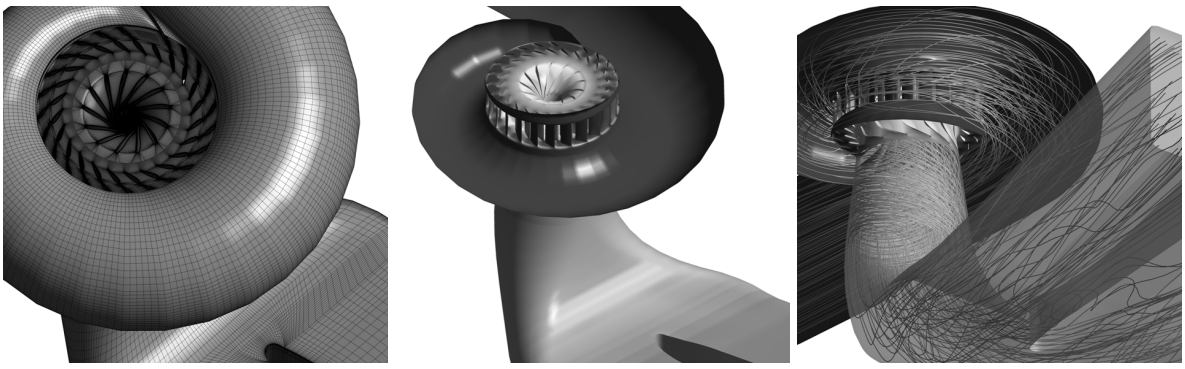

**(a)** **(b)** **(c)**

**Figure 2.1:** Rated operating condition showing: **(a)** computational grid, **(b)** hydraulic surfaces coloured by pressure magnitude ($p$) and **(c)** flow streamlines through the machine

The numerical parameters were tested with the individual components and then used for the complete machine simulation. The mesh density was varied until grid independent results and $y^+$ values in the logarithmic region, between 30 and 200, were obtained.

For the spiral case, the mesh refinement went from approximately 500 thousand to 800 thousand cells, for one blading passage, i.e. stay vane, guide vane and runner, from 80 thousand to 300 thousand and for the draft tube from 270 thousand to 550 thousand. The maximum deviation with the finest grid, taking into account all simulated points and all measured values, was 1,6%, as seen in Table 2.1, whereas the maximum deviation with the coarsest mesh was 3,4%.

Distinct interpolation schemes were also evaluated. As expected UDS and CDS resulted in inaccurate velocity and pressure distribution fields, as well as deviations in the efficiency values up to 5,1%. The second-order schemes MINMOD and QUICK delivered the most accurate results for all measured quantities. However, the former showed superior convergence behaviour when compared to the latter and was used to obtain the results in Table 2.1.

The standard $k$-$\varepsilon$, $k$-$\varepsilon$ LCL, $k$-$\omega$ and $k$-$\omega$ SST turbulence models were also considered for the steady state simulations. The models based on the eddy-dissipation equation provided the best results and the fastest convergence rate. Due to the nonlinear formulation of the $k$-$\varepsilon$ LCL turbulence model, the computations using it were more than 30% slower than with the standard $k$-$\varepsilon$ model, with no noticeable accuracy improvement. Although the $k$-$\omega$ models produced acceptable results, with maximum deviation of 3,0%, its numerical stability and convergence were poorer. Since the inlet turbulence content is of difficult experimental determination, the prescribed inlet turbulence intensity was varied in the numerical tests from 1% up to 10%. Nevertheless, it yielded negligible variations on the calculated values, possibly because of the long inlet pipe, about 2,5 times the spiral case inlet diameter, and the significant turbulence production in the turbine.

In addition to the prescribed turbulence intensity, the total volume flow completed the boundary conditions set at the spiral case inlet section. At the outlet, the computational domain extension was varied, in order to avoid boundary effects and inaccuracies at the draft tube end, where the velocity and pressure fields are still of interest. As studied by Mauri [12], a rectangular extension of the outlet section was employed, with an extent of one third of the draft tube plan projected length. The pressure was fixed to a reference level at the outlet section.

**Table 2.1:** Experimental results obtained at the model test and numerically simulated results.

| | Model Test | | | | Simulation | | | | Deviation | | | |
|---|---|---|---|---|---|---|---|---|---|---|---|---|
| Operating Point | $n'_1/n'_{1_{opt}}$ [%] | $Q'_1/Q'_{1_{opt}}$ [%] | $T'_1/T'_{1_{opt}}$ [%] | $\eta/\eta_{opt}$ [%] | $n'_1/n'_{1_{opt}}$ [%] | $Q'_1/Q'_{1_{opt}}$ [%] | $T'_1/T'_{1_{opt}}$ [%] | $\eta/\eta_{opt}$ [%] | $\delta n'_1$ [%] | $\delta Q'_1$ [%] | $\delta T'_1$ [%] | $\delta\eta$ [%] |
| Optimum | 100,0 | 100,0 | 100,0 | 100,0 | 99,4 | 100,0 | 100,3 | 100,2 | -0,6 | $< 0,1$ | 0,3 | 0,2 |
| Rated | 110,3 | 111,5 | 108,3 | 97,2 | 109,6 | 111,5 | 110,0 | 98,7 | -0,6 | $< 0,1$ | 1,6 | 1,5 |
| Normal | 107,0 | 103,0 | 102,2 | 99,3 | 106,0 | 103,0 | 102,4 | 99,4 | -1,0 | $< 0,1$ | 0,2 | 0,1 |
| High Head | 107,8 | 73,9 | 69,3 | 93,8 | 106,7 | 73,9 | 69,3 | 93,8 | -1,0 | $< 0,1$ | 0,0 | 0,0 |
| Low Head | 119,9 | 70,8 | 64,4 | 91,0 | 119,0 | 70,8 | 65,1 | 91,9 | -0,7 | $< 0,1$ | 1,0 | 1,0 |

Table 2.1 shows the simulation results, obtained with the described numerical model and parameters. The computed head, flow, torque and efficiency were compared to the experimental values, measured at the test rig, in terms of dimensionless normalized parameters: $n'_1/n'_{1_{opt}}$, $Q'_1/Q'_{1_{opt}}$, $T'_1/T'_{1_{opt}}$ and $\eta/\eta_{opt}$. Considering the maximum deviation of 1,6%, the numerical model was judged to be enough accurate for the further simulation steps dealing with pressure pulsations, rotor-stator interaction, vortex shedding and flow instabilities.

To represent the evaluation of the computational codes, the pressure coefficient distribution, at the rated operating condition, calculated with NS3D and CFX, was plotted in Figure 2.2 over the normalized blade surface length at three conformal planes. The deviations between the two codes were minimal.

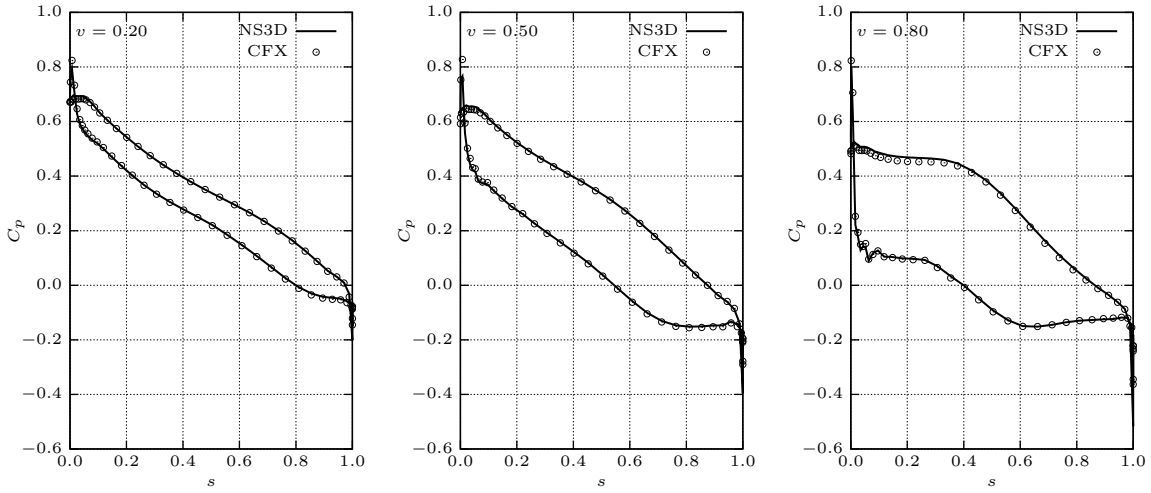


**Figure 2.2:** Pressure coefficient distribution ($C_p$) calculated with NS3D and CFX over the normalized blade surface length ($s$), measured from the blade leading edge, at three conformal planes and normalized coordinates ($v$), measured from the crown to the band.

For the transient simulations of the complete machine, different time step sizes were considered and the results sensitivity to it was tested. Using 118 time steps per machine revolution was enough to reproduce the overall flow behaviour through the complete turbine. However, at this condition, the rotor-stator interaction could not be represented in detail. To obtain adequate resolution in time for the interaction between the guide vanes and the runner, 392 time steps per machine revolution were used, resulting in average 30,2 time steps per runner blade passage and 16,3 time steps per guide vane passage.

For capturing the vortex shedding effect at the runner trailing edges, the time resolution requirement was even tougher and 5882 time steps per machine revolution had to be employed. As long as the vortex shedding phenomenon showed to have no influence in the overall flow pattern and due to its excessive time step requirements, the first machine revolutions were computed with the larger time step size of 392 time steps per revolution, until the flow became stable in the complete turbine and its overall dynamic

characteristics could be evaluated. Afterwards, the time step size was reduced to 5882 time steps per machine revolution and the simulation was carried out further on, until the set in of the von Kármán vortex streets at the runner trailing edges. The main flow though all turbine components was only stabilized after all the initial fluid volume had left the machine outlet section, which corresponded, in this case, to approximately 34 machine revolutions.

The time step size had a direct impact in the total elapsed time for the numerical computations. On one hand, the reduced time step size implies in a large number of discretization points in time for a machine rotation, on the other hand, fewer iterations are needed to achieve convergence within a given time step. Using 392 time steps per machine revolution was about 8 times faster than with 5882 and about twice slower than with 118. As a reference for the computation speed, in a Linux cluster with 8 Intel Q6600 processors, each with 4 kernels, 2,4 GHz and 2 GB memory, 1,7 machine rotations per day could be computed.

The numerical procedure for solving the transient time steps was tested as well. As stated by Ferziger, Perić [6], multigrid methods brought no acceleration to the numerical solution of the transient fluid flow equations. The BCGSTAB solution method was as fast as the multigrid method, with the additional advantage of introducing no artificial numerical oscillations in the computed pressure transient signals. Its better numerical stability is possibly related to the very different turbulent scales present in the complete machine simulation, as for example on the runner blades in contrast to the draft tube. The last test related to the solution of the transient fluid motion equations dealt with the use of double or single computational precision. No deviation could be identified in the results obtained with single or double precision. Therefore, the simulations were carried out with single precision, with the advantage that it ran twice as fast as with double precision.

# 3 Results

After the extensive verification of the numerical model, the focus was transferred to the investigation of the pressure oscillations in the turbine runner, arising from the rotor-stator interaction, from the vortex shedding at the runner trailing edge and from the flow instabilities in the draft tube diffusor. At this point, the effect of the URANS and LES based turbulence models on the pressure pulsation pattern and magnitude was analysed. The experimental determination of the oscillating pressure field at the runner is not common. Nevertheless, it is responsible for the dynamic structural load at the runner and, thus, it is required for an accurate calculation of the dynamic structural stresses. The current CFD model allowed the numerical computation of the fluid flow transient effects, providing the pressure dynamic distribution in the complete machine, including the turbine runner. Since the modelling of turbulence can significantly affect the transient characteristics of the simulated flow, the results obtained using URANS, SAS and DES were compared.

As seen in Figure 3.1, the pressure oscillations at the runner, for operating conditions near to the optimum and to the rated point, were dominated by the rotor-stator interaction, which was caused by the kinematic interaction between the moving runner blades and the stationary guide vanes, stay vanes and spiral case. Apart from this kinematic effect, turbulent phenomena and flow instabilities could hardly be associated to it, at these stable operating conditions.

**(a)** **(b)** **(c)**

**Figure 3.1:** Pressure oscillation amplitude, caused by the main flow, at the rated operating condition, at three conformal planes and normalized coordinates **(a)** $v = 0,20$, **(b)** $v = 0,50$ and **(c)** $v = 0,80$.

As an example, the transient pressure at the runner leading edge near to the band, and its Fourier transform, are represented in Figure 3.2, for the rated point. The passage of one runner blade by each of the 24 guide vanes can be identified in the transient pressure signal, as well as the effect of the inhomogeneous pressure distribution along the spiral case. This effect is reflected in the Fourier transform by local maximum peaks located at 1 and 24 times the machine rotating frequency. For the considered construction concept and machine specific speed, it was observed that, near to the

crown, the pressure oscillations were mainly due to the interaction between the runner and the spiral case inhomogeneous pressure distribution, while, near to the band, it was mostly caused by the interaction between the runner blades and the guide vanes, because of the small distance between them at this region. The amplitudes presented in the frequency domain were smaller as in the time domain, because of the intensity distribution over a frequency range, in opposition to a pure sinusoidal curve.

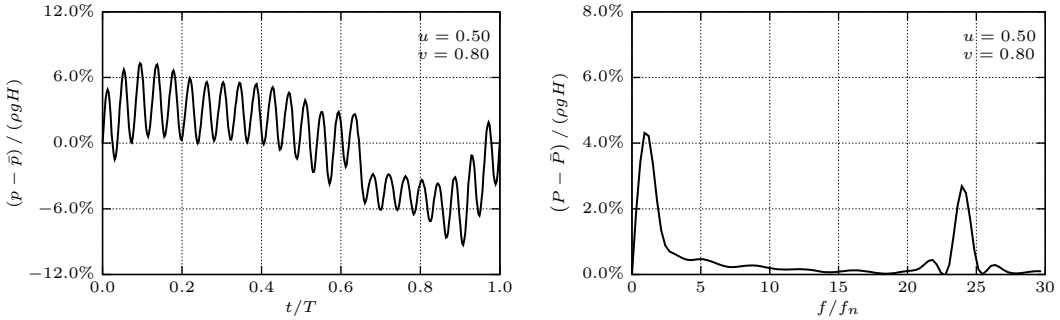


**Figure 3.2:** **(a)** Pressure oscillation amplitude over one rotation period, at the rated operating condition, at the runner blade leading edge near to the band and its **(b)** Fourier transform, normalized in relation to the rotational frequency.

The overall pressure oscillation amplitude, defined as the half peak to peak value, at the blade surface is represented in Figures 3.3 and 3.4. In most part of the blade surface, the pressure pulsation amplitude was between 0,3% and 2,1% of the net head, for the rated operating condition. It could only achieve 12,4% in the close vicinity of the leading edge near to the band. These are typical values also encountered in [3, 5, 14]. Nonetheless, if the pressure oscillation amplitude is referred to the local time averaged pressure, instead of the net head, it can reach considerably higher values, ranging from 0,8% to 51,4%, approaching or exceeding 10,0% in larger portions of the blade surface. This kind of referencing appears to be interesting, since the local time averaged pressure and the local pressure oscillation amplitude are respectively responsible for the static and dynamic structural loads.

Considering the other transient effects in the flow simulation, beginning by the vortical structures in the draft tube diffusor, generated by the flow instabilities at part load, they could only be captured using the SAS and DES turbulence models and not with the URANS. This shortcoming was already expected, because of the excessive dissipation introduced by URANS in transient simulations, and, in this case, avoiding the set in of the vortex rope in the draft tube diffusor. Figure 3.5 presents the vortex rope simulated with the SAS turbulence model confronted to the model test observation and Figure 3.6 compares the pressure oscillation amplitude computed with the URANS and SAS turbulence models. Even if the studies concentrated on the runner dynamic load, the computed pressure pulsation amplitude in the diffusor, going from 8,6% to 13,1% along its circumference, could indicate the accuracy of the CFD model, when compared

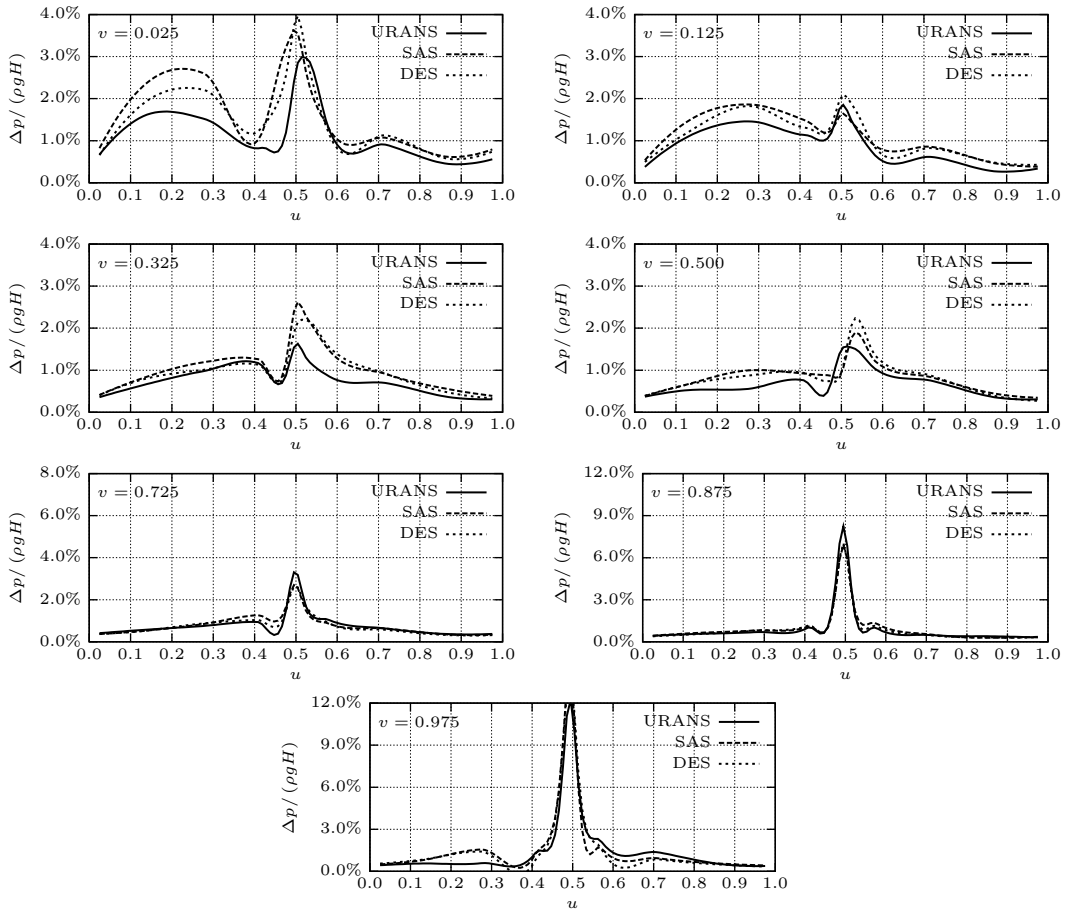


**Figure 3.3:** Pressure oscillation amplitude, caused by the main flow, at the rated operating condition, along the normalized blade length ($u$), measured from the pressure side trailing edge to the suction side trailing edge, at selected conformal planes ($v$).

to the model test values, between 9,0% to 13,5%, at this operating condition. Since the diffusor vortex was the driving transient effect at part load and it was not captured by the URANS turbulence model, the calculated pressure oscillation amplitudes, simulated under this condition, presented only the influence of the rotor-stator interaction, with considerably small values, between 0,1% and 1,2% of the net head in the most part of the blade and 3,9% at the leading edge near to the band. On the other hand, the other tested turbulence models, as the SAS for example, could yield values of the same magnitude as [5], from 0,6% up to 5,0% of the net head. The highest amplitudes could be observed at considerable extents of the blades, especially at their suction sides, because of their relative position and proximity to the draft tube diffusor. Even if the pressure oscillation amplitudes generated at part load were higher as at the rated operating condition, it should be considered that extreme partial load operation is not as frequent as the operation near to the optimum and rated points and, therefore, its real importance should be carefully evaluated.

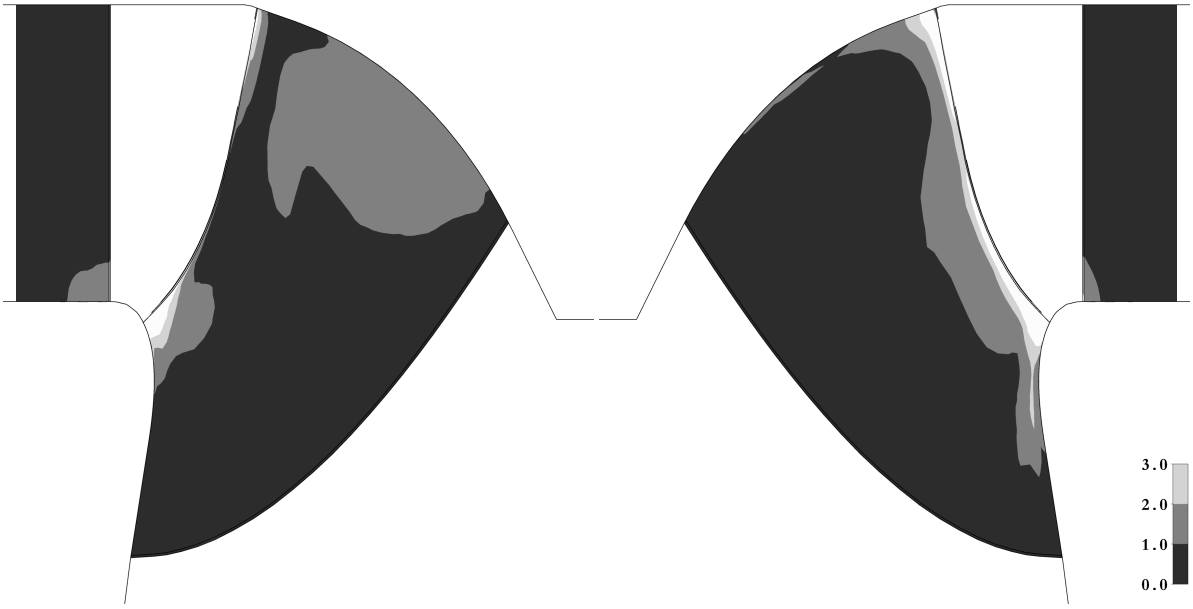


**Figure 3.4:** Normalized pressure oscillation amplitude, in percent, at the rated operating condition, caused by the main flow. Meridian view.

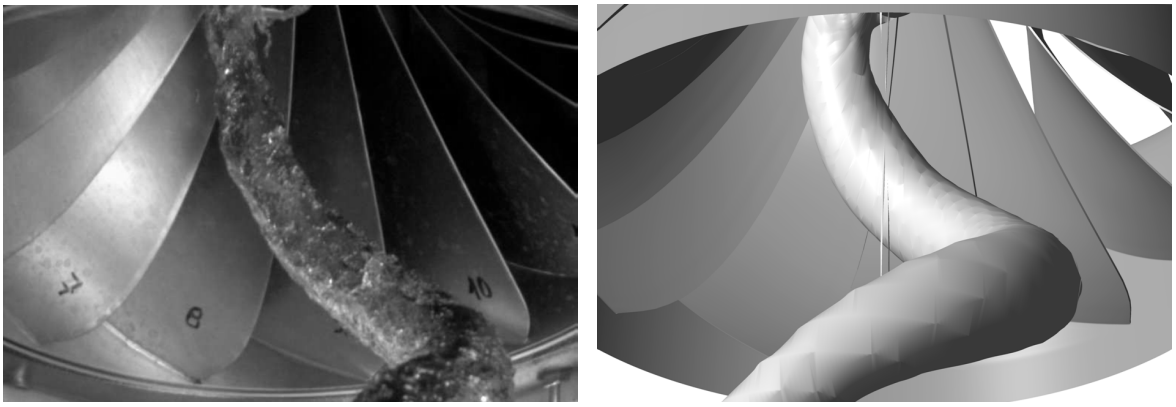

**(a)** **(b)**

**Figure 3.5:** Cavitating vortex cores at part load at low head: **(a)** observed during the model test, **(b)** computed with the SAS turbulence model during the transient simulation of the complete turbine.

Moving on to the last investigated transient effect, the vortex shedding at the runner trailing edges could not be clearly recognized in the main flow, as a result of its secondary flow nature and its much higher frequency. Though, concentrating on the trailing edge region, the pressure oscillation caused by the vortex street could be identified, as in Figures 3.7 and 3.8. Its oscillation amplitude, going from 0,9% to 3,7% of the net head, cannot be neglect. These values are higher than the overall pressure pulsation in most part of the blade, at the rated operating condition, and approach the part load calculated amplitudes. Even though it is limited to a small restricted area, it is

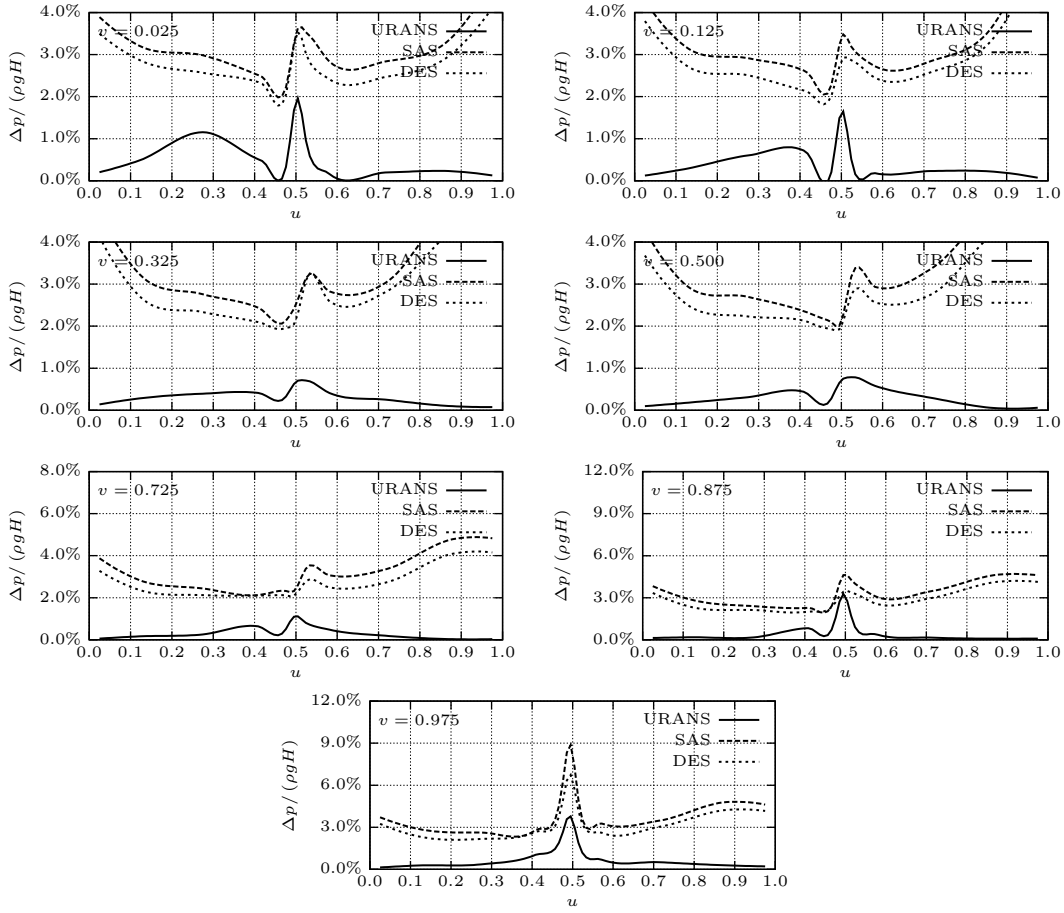


**Figure 3.6:** Pressure oscillation amplitude, caused by the main flow, at part load and low head, along the normalized blade length ($u$), measured from the pressure side trailing edge to the suction side trailing edge, at selected conformal planes ($v$).

located where the structure stiffness is weakest and it can possibly excite blade vibration mode shapes [7]. Moreover, the investigated vortex shedding occurs at the rated point and at operating conditions near to it, appearing to be more frequent than the part load effects, for example. The vortex generation was not synchronous along all the trailing edge extension, possibly because of the local flow conditions, as stream velocity, boundary layer thickness and deviation angle. It presented calculated frequencies of 148 times the rotating frequency along the lower half blade extension and of 86 times the rotating frequency at the upper third part of the blade. In contrast to the rotor-stator interaction and similar to the draft tube instabilities, the simulated vortex shedding was strongly affected by the turbulence model, as indicated in Figure 3.9. The URANS turbulence model delivered too small pressure oscillation amplitudes when compared to SAS and DES. Besides from its theoretical higher precision, the simulations with DES and SAS presented the most coherent vortical structures for the von Kármán vortex streets and the best agreement with the experimental observations in Figure 3.10.

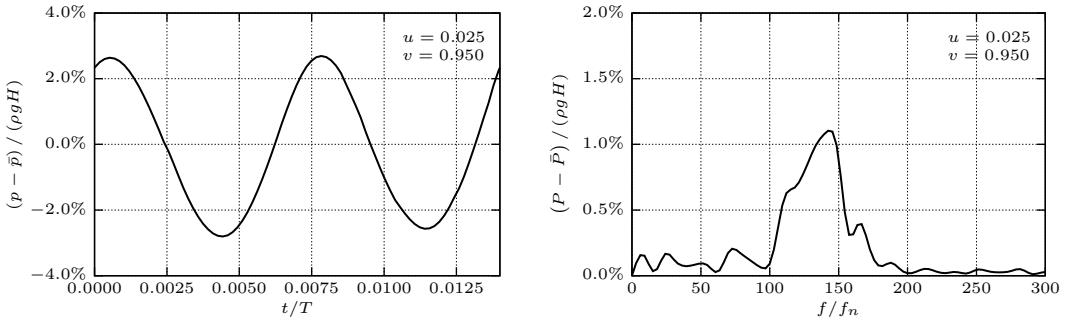


**(a)** **(b)**

**Figure 3.7:** **(a)** Pressure oscillation amplitude, at the rated operating condition, induced by the vortex shedding effect, at the runner trailing edge near to the band and its **(b)** Fourier transform.

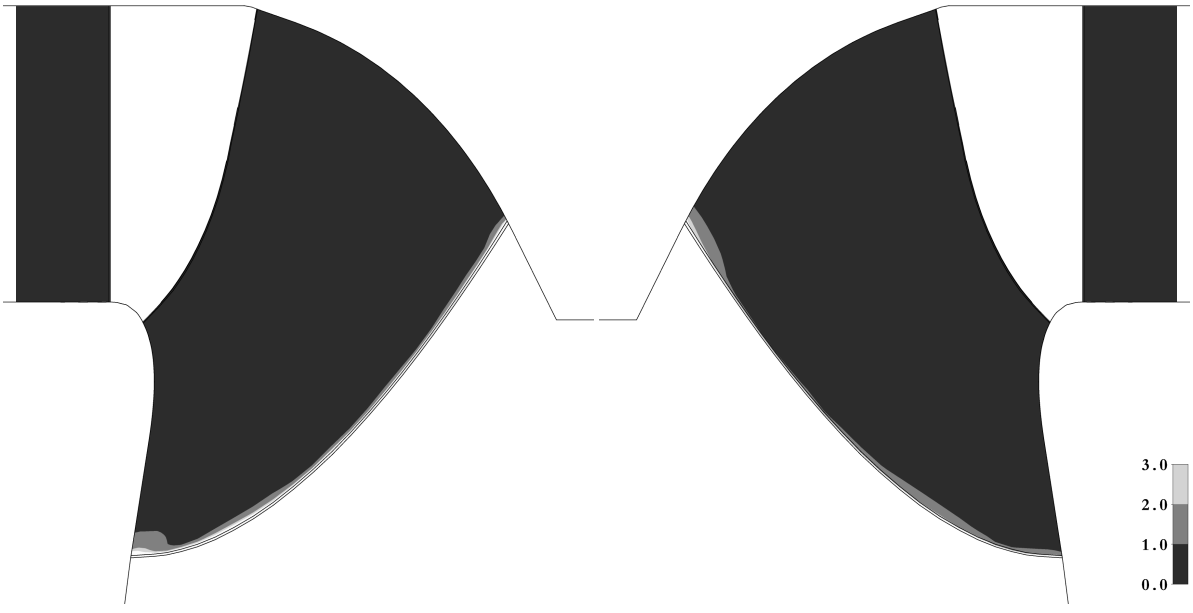


**Figure 3.8:** Normalized pressure oscillation amplitude, in percent, at the rated operating condition, induced by the vortex shedding effect. Meridian view.

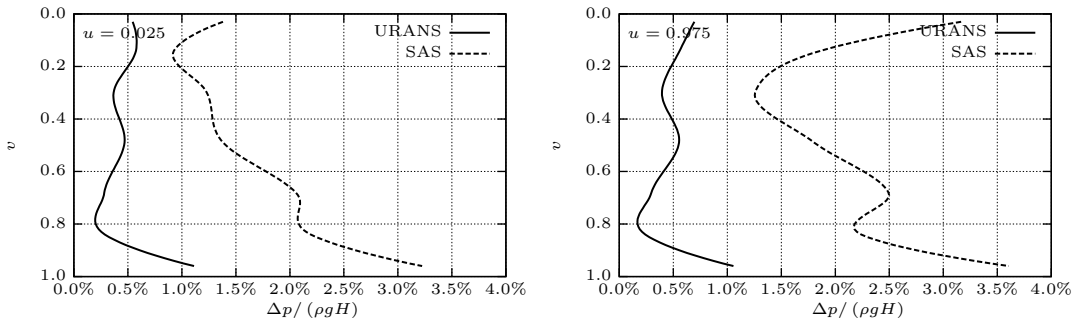


**(a)** **(b)**

**Figure 3.9:** Pressure oscillation amplitude, induced by the vortex shedding effect, at the rated operating condition, along the runner trailing edge at **(a)** the pressure and **(b)** suction sides, calculated with different turbulence models.

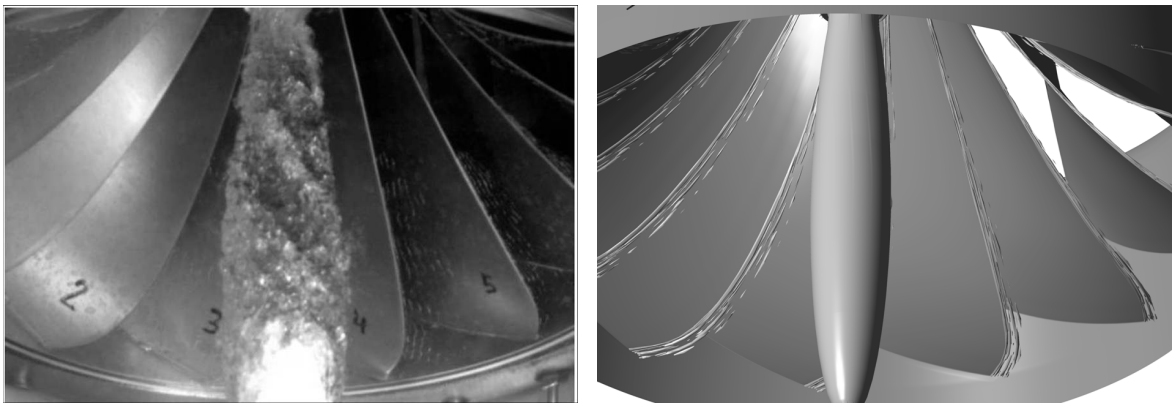

**(a)** **(b)**

**Figure 3.10:** Cavitating vortex cores at the rated operating condition **(a)** observed during the model test and **(b)** computed with SAS during the transient simulation of the complete turbine.

# 4 Conclusions

The transient simulation of the fluid flow through the complete turbine offered the possibility to predict the oscillating pressure field in a high specific speed Francis turbine. The pressure pulsations are at the origin of the structural stresses, which may cause the runner mechanical failure, and its numerical simulation allows more precise structural computations, improving the prediction of the dynamic stresses, fatigue strength and durability.

Although the vortex shedding at the runner trailing edges is a secondary flow effect, the numerical computations pointed out that it can also produce high amplitude pressure oscillations, comparable to the ones arising from the rotor-stator interaction and from the flow instabilities in the draft tube diffusor. In spite of the difficult numerical calculation of the vortex shedding effect, the flow simulation results and the phenomenon occurrence at the runner structure weakest region suggests that it should be considered in the runner structural assessment.

In relation to the numerical CFD model, the simulations carried out with NS3D and CFX showed close agreement with the available experimental results. As already expected, different turbulence models had not the same effect on the numerical results. While the URANS, SAS and DES turbulence models could all properly reproduce the dynamic characteristics of the flow at the optimum, rated and normal operating conditions, only SAS and DES were able to capture the vortex rope in the draft tube diffusor at partial load operation. The vortex shedding pressure oscillations could be identified by all turbulence models. However, only SAS and DES could simulate the coherent von Kármán vortex street, with the adequate pressure pulsation amplitude.

The main future steps in this study will be the transient computational structural analysis of the runner, using the pressure distribution calculated at each time step of the flow simulation. Thereby, the eventual accuracy gains in the structural calculation and the influence of the rotor-stator interaction, draft tube instabilities and vortex shedding on the runner structure will be evaluated. Other investigations will consider more operating points, will evaluate the effect of numerical parameters on the SAS and DES turbulence models, verify the adequacy of theoretical models based on the Strouhal number to predict the vortex shedding phenomenon and better study the influence of the draft tube instabilities on the upstream flow.

## References

[1] Antonsen, Ø. Ustabile driftsområder for Francisturbiner. Tech. rep., Norges Teknisk- Naturvitenskaplige Universitet, Trondheim, Norway, 2005.

[2] Ausoni, P. Etude du mécanisme de génération des tourbillons de von Kármán et de leurs interactions avec la structure. Tech. rep., Ecole Polytechnique Fédérale de Lausanne, Lausanne, Switzerland, 2004.

[3] Avellan, F., Etter, S., Gummer, J. H., and Seidel, U. Dynamic Pressure Measurements on a Model Turbine Runner and their Use in preventing Runner Fatigue Failure. In *Proceedings of the 20th IAHR Symposium* (Charlotte, North Carolina, USA, 2000).

[4] Coutu, A., Proulx, D., Coulson, S., and Demers, A. Dynamic Assessment of Hydraulic Turbines. In *Proceedings of HydroVision 2004* (Montréal, Quebec, Canada, 2004).

[5] Farhat, M., Avellan, F., and Seidel, U. Pressure Fluctuation Measurements in Hydro Turbine Models. In *Proceedings of the 9th Symposium on Transport Phenomena and Dynamics of Rotating Machinery* (Honolulu, Hawaii, USA, 2002).

[6] Ferziger, J. H., and Perić, M. *Computational Methods for Fluid Dynamics*, 3rd ed. Springer-Verlag, Berlin, Germany, 2002.

[7] Fischer, R., Seidel, U., Grosse, G., Gfeller, W., and Klinger, R. A Case Study in Resonant Hydroelastic Vibration: The Causes of Runner Cracks and the Solutions Implemented for the Xiaolangdi Hydroelectric Project. In *Proceedings of the 21st IAHR Symposium* (Lausanne, Switzerland, 2002).

[8] Harten, A. High resolution schemes for hyperbolic conservation laws. *Journal of Computational Physics 49*, 3 (1983), 357–393.

[9] Huth, H. J. *Fatigue Design of Hydraulic Turbine Runners*. PhD thesis, Norges Teknisk- Naturvitenskaplige Universitet, Trondheim, Norway, 2005.

[10] Kuntz, M., Garcin, H., Guedes, A., Menter, F., Parkinson, E., and Kueny, J. L. Developments of CFX-TASCflow for unsteady rotor-stator simulations in the frame of the European project HPNURSA. In *CFX Users Conference 2000* (Munich, Germany, 2000).

[11] Lien, F. S., Chen, W. L., and Leschziner, M. A. Low-Reynolds-number eddy-viscosity modelling based on non-linear stress-strain/vorticity relations. In *Proceedings of the 3rd Int. Symposium on Engineering Turbulence Modelling and Experiments, Crete, Greece* (Amsterdam, Netherlands, 1996), W. Rodi, Ed., Elsevier, pp. 91–100.

[12] Mauri, S. *Numerical Simulation and Flow Analysis of an Elbow Diffuser*. PhD thesis, Ecole Polytechnique Fédérale de Lausanne, Lausanne, Switzerland, 2002.

[13] Menter, F. R., and Egorov, Y. A Scale-Adaptive Simulation Model using Two-Equation Models. Tech. Rep. 2005-1095, AIAA, Reno, Nevada, USA, 2005.

[14] Nennemann, B., Vu, T. C., and Farhat, M. CFD prediction of unsteady wicket gate-runner interaction in Francis turbines: A new standard hydraulic design procedure. In *Waterpower XIV* (Austin, Texas, USA, 2005).

[15] Ruprecht, A., Kirschner, O., Lippold, F., and Buntić, I. Noise reduction in a small Francis turbine caused by vortex shedding at the trailing edge, numerical analysis and field test. In *IAHR 11th International Meeting of the Work Group on the behaviour of hydraulic machinery under steady oscillatory conditions* (Stuttgart, Germany, 2003).

[16] Strelets, M. Detached Eddy Simulation of Massively Separated Flows. In *39th Aerospace Sciences Meeting and Exhibit* (Reno, Nevada, USA, 2001), no. 2001-0879, AIAA.

# A Blade Coordinate System

The Figure A.1 shows the coordinate system used for the blade. The $u$ coordinate runs along the blade surface, at a given conformal plane, starting from the blade trailing edge on the pressure side ($u = 0$), passing through the leading edge ($u = 0,5$) and arriving at the blade trailing edge on the suction side ($u = 1$). The $v$ coordinate describes the other surface direction and runs perpendicular to the conformal planes, from the crown ($v = 0$) to the band ($v = 1$). The $s$ coordinate is similar to the $u$ coordinate, but starts at the blade leading edge ($s = 0$) and reaches the blade trailing edge ($s = 1$). It is used for the pressure and suction sides.

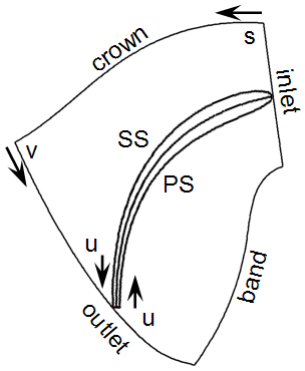


**Figure A.1:** Blade coordinate system.